



Available online at www.sciencedirect.com

ScienceDirect

Comput. Methods Appl. Mech. Engrg. 357 (2019) 112567

Computer methods in applied mechanics and engineering

www.elsevier.com/locate/cma

An inverse modeling approach for predicting filled rubber performance

Jiaying Gao^a, Modesar Shakoor^a, Hiroshi Jinnai^b, Hiroshi Kadowaki^c, Eisuke Seta^c, Wing Kam Liu^a,*

^a Northwestern University, 2145 Sheridan Road, Evanston, IL, 60208, United States of America
^b Institute of Multidisciplinary Research for Advanced Materials, Tohoku University, Sendai, Miyagi, 980-8577, Japan
^c Bridgestone Corporation, 3-1-1 Ogawahigashi-cho, Kodaira-shi, Tokyo, 187-8531, Japan

Received 5 April 2019; received in revised form 11 July 2019; accepted 25 July 2019 Available online 9 August 2019

Highlights

- A comprehensive computational framework for predicting filled rubber properties.
- Detailed experimental characterization of the filled rubber microstructure.
- Filled rubber interphase inverse modeling for accurate property prediction.
- Filled rubber property prediction with order reduction (52,631 speed-ups than FEM).

Abstract

In this paper, a computational procedure combining experimental data and interphase inverse modeling is presented to predict filled rubber compound properties. The Fast Fourier Transformation (FFT) based numerical homogenization scheme is applied on the high quality filled rubber 3D Transmission Electron Microscope (TEM) image to compute its complex shear moduli. The 3D TEM filled rubber image is then compressed into a material microstructure database using a novel Reduced Order Modeling (ROM) technique, namely Self-consistent Clustering Analysis (a two-stage offline database creation from training and learning, followed by data compression via unsupervised learning, and online prediction approach), for improved efficiency and accuracy. An inverse modeling approach is formulated for quantitatively computing interphase complex shear moduli in order to understand the interphase behaviors. The two-stage SCA and the inverse modeling approach formulate a three-step prediction scheme for studying filled rubber, whose loss tangent curve can be computed in agreement with test data. © 2019 Elsevier B.V. All rights reserved.

Keywords: Nano-composites; Interphase; Database for self-consistent clustering analysis (SCA); Two stage offline-online reduced order modeling

1. Introduction

Composite materials in general exhibit improved mechanical behaviors compared to their basic constituents. Such characteristics provide a window for creating specific materials to satisfy requirements that are hard to meet

E-mail address: w-liu@northwestern.edu (W.K. Liu).

Corresponding author.

by materials without specific treatments. It is well-known that the properties of Polymer Nano-Composites (PNCs) differ from pure polymer components partly due to an interphase region between polymer and filler [1–4]. Thus, it is possible to design specific properties by adding fillers into polymer components (such as rubber compounds) to achieve different viscoelastic behaviors compared to pure polymers without fillers [5,6]. In this manuscript, a computational framework for the efficient evaluation of filled rubber properties and interphase property inverse modeling for improving filled rubber properties prediction is proposed.

In the rubber and tire industry, reduction of loss tangent (or $tan(\delta)$) can reduce rolling resistance whereas an increase of loss tangent provides more friction between the tire and the ground. Experimental studies reveal that fillers in polymer compounds indeed result in different viscoelastic behavior [7,8] for PNC vs. pure polymer compound. For styrene-butadiene rubber, the addition of carbon black filler reduces $tan(\delta)$ in the low-temperature region but increases $tan(\delta)$ in the high-temperature region [8]. Moreover, Brinson et al. conducted a study of styrene-butadiene rubber with different fillers and concluded that fillers enhanced the overall rigidity of the PNC but reduced $tan(\delta)$ [9]. Therefore, various tire properties can be achieved through custom designed polymer nano-composite (PNC), or filled rubber.

The cause of change in viscoelastic behavior between PNC and the pure polymer has been studied extensively. Due to the exponential growth of computational power over the past decades, researchers are able to utilize computational methods, such as Finite Element Methods [6,10], Meshless methods [11], and Molecular Dynamics (MD) simulations [12–15], to capture the effect of fillers in polymer compounds by observing the interaction between polymer chains and fillers. Polymer chains aggregate around added filler material, creating a denser layer of polymers. Such results are due to van der Waals interactions between polymers and fillers. Results obtained from MD agree well with experimental observations in [2,9], where the interphase exhibits stiffer responses compared to the polymer matrix. To characterize such a change of polymer structure, the interphase can be used to distinguish different viscoelastic behaviors of PNC and pure polymer compound. In this work, a filled polymer system using a three-phase model, adopted in micromechanical analysis of PNC [16,17], is considered: these phases are the filler, interphase, and polymer. The three-phase model is applied to the filled rubber sample studied in the present work; this model should be able to capture the difference in viscoelastic performance between filled and unfilled rubber.

Previous works performed by Jinnai et al. [18,19] utilize high-resolution 3D transmission electron microtomography (3D TEM) to reconstruct the fine microstructure of a PNC with sub-nanometer resolution. The reconstructed images allow the effect of the microstructure to be accurately accounted for when computing the overall behavior of the filled rubber.

Rubber properties can be experimentally measured by dynamic mechanical analysis (DMA). The experimental procedures provide viscoelastic properties, i.e., storage and loss moduli, of the rubber compound. As a result, DMA provides overall homogenized properties of the rubber. Numerically, macroscopic properties can be determined through various homogenization approaches. The aforementioned 3D TEM process has been applied to a different filled rubber geometry, which has already been studied via the Finite Element (FE) method to obtain the local stress response [6]. However, in this past work, the filled rubber geometry provided by 3D TEM as a 3D digital image was converted to a fine conforming FE mesh, which could only be used on a supercomputer. Voxel meshes of large sizes, such as 3D digital images provided by 3D TEM, are more suitable for computational homogenization using the Fast Fourier Transform (FFT) based numerical method, as noted by [20]. The digital image can be directly used in the FFT based algorithm to solve for local and overall responses under designated macroscopic boundary conditions, as discussed in [21,22]. Therefore, the properties of the filled rubber can be directly obtained via the FFT algorithm by using the 3D image of the filled rubber.

The existing experimental techniques allow measurement of $tan(\delta)$ curves (also known as master curves), of filled and unfilled rubber through DMA. Therefore, if the filled rubber is assumed to be a two-phase model with rubber and filler phases, it is possible to conduct a numerical simulation of its responses at different frequencies using measured properties of unfilled rubber and filler. In the present work, the property of interphase is unknown, which makes it hard to predict the filled rubber's master curve through basic constituents: unfilled rubber and filler. In this paper, we combined interphase modeling via the so-called inverse modeling technique [23] and an efficient FFT-based homogenization scheme to compute the master curve of a filled rubber using a fine mesh reconstructed from 3D TEM. The master curve is validated by experimental results to illustrate the efficacy of our proposed scheme. Comparison of the FFT method and a recently proposed Self-consistent Clustering Analysis (SCA) is performed to examine the improved computational efficiency of this reduced order modeling-based approach.

 Table 1

 Formula of rubber samples (weight ratio per hundred rubber).

	Unfilled rubber sample	Filled rubber sample
Isoprene (IR2200)	100	100
Sulfur (cross-linking agent)	1.5	1.5
Other agents	9.3	9.3
Silica (Zeosil [®] 1165 MP)	None	40

The paper is organized as follows. Section 2 focuses on the experimental study of filled rubber and 3D TEM reconstruction of a filled rubber sample. Section 3 provides details on the FFT algorithm employed. Section 4 introduces the SCA method. Section 5 introduces the inverse modeling scheme for interphase properties computation. Section 6 provides results and discussion. The major contribution of the current work is to demonstrate an efficient integrated experimental and modeling approach that combines the merits of an FFT homogenization algorithm and data-driven SCA with an inverse modeling technique. With 3D TEM reconstruction of a filled rubber sample and experimental DMA data, we aim to build an understanding of interphase properties in filled rubber components.

2. Experimental study of the filled rubber

2.1. Preparation of unfilled and filled rubber samples

The unfilled rubber sample used in the present study is made of poly-isoprene (IR2200) with some chemical agents such as sulfur, stearic acid, microcrystalline wax, zinc oxide, etc. In the first stage of mixing, poly-isoprene and agents other than curing agents were mixed. Then curing agents, such as sulfur, were added. The mixture of polymer and agents was cured with a high temperature to obtain a vulcanized unfilled rubber sample. The filled rubber sample is made of poly-isoprene, silica particles (Zeosil 1165MP), and some chemical agents. It was obtained in the same way except that silica particles are added in the first stage of mixing. The formula of these rubber samples is summarized in Table 1.

2.2. Experimental results on master curve measurements of filled and unfilled rubber samples

Storage and Loss modulus of filled and unfilled rubber samples were measured by a dynamic mechanical analysis (DMA) (TA Instruments, rubber rheometer ARES-G2). Cylindrical samples with a diameter of 8 mm and a height of 6 mm were used. The measurements were operated at 0.1% oscillatory shear strain in which the material response is in the linear viscoelasticity region. In order to obtain the viscoelastic responses in a wide frequency range, a frequency sweep from 0.5 Hz to 50 Hz was operated at a temperature range of -60 °C to 40 °C. Master curves were obtained by time–temperature superposition with the reference temperature of 25 °C where only horizontal shift was performed. It is clearly indicated in Fig. 1 that the temperature dependence of the horizontal shift factor aT is well described by the Williams–Landel–Ferry (WLF) equation [24]. Figs. 2, 3, and 4 show the storage shear modulus, loss shear modulus, and loss tangent of these samples respectively.

2.3. 3D-TEM reconstruction of filled rubber sample

The filled rubber was made into thin sections with ~ 100 nm thickness using a focused ion beam (JEOL, JEM-9310FIB) at a cryogenic temperature of -150 °C. The ultrathin section was transferred onto a Cu mesh grid with a polyvinyl formal supporting membrane. Prior to the electron microscopy experiments, gold particles 5 nm in diameter were placed on the ultrathin section from colloidal aqueous solution.

We conducted 3D observations by TEM and 3D-TEM using a JEM-2200FS microscope (JEOL, Ltd., Japan) operated at 200 kV. The electron microscope was equipped with a slow-scan USC 4000 CCD camera (Gatan, Inc., USA). Elastically scattered electrons (electron energy loss: 0 ± 40 eV) were selected by an energy filter installed in the microscope (Ω filter, JEOL Ltd., Japan).

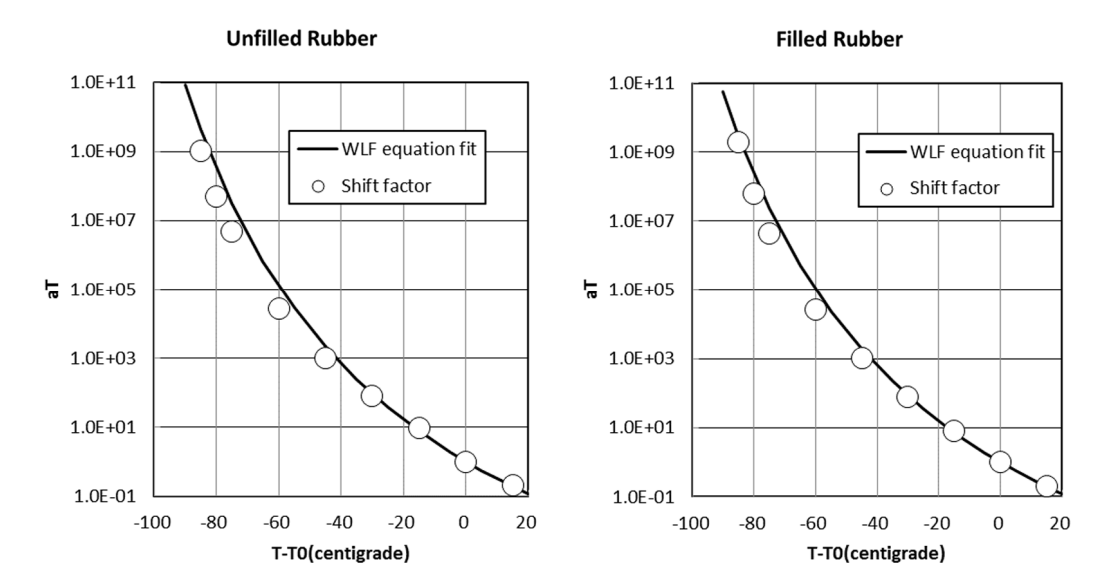


Fig. 1. Left: Temperature dependence of horizontal shift factor for unfilled rubber. Right: Temperature dependence of horizontal shift factor for filled rubber. aT, T and T0 stand for horizontal shift factor, temperature, and reference temperature respectively.

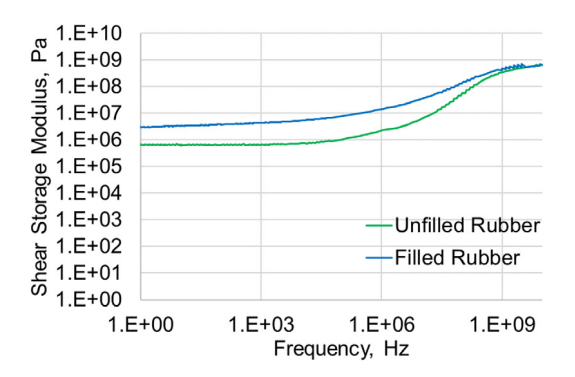


Fig. 2. Measured shear storage modulus of unfilled rubber and filled rubber.

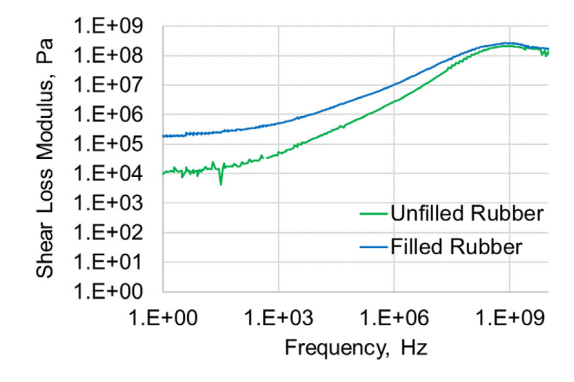


Fig. 3. Measured shear loss modulus of unfilled rubber and filled rubber.

A series of TEM images were acquired at tilt angles in the range of -66° to 73° at an angular interval of 1° . Subsequently, the tilt series of the TEM images were aligned by the fiducial marker method, using gold

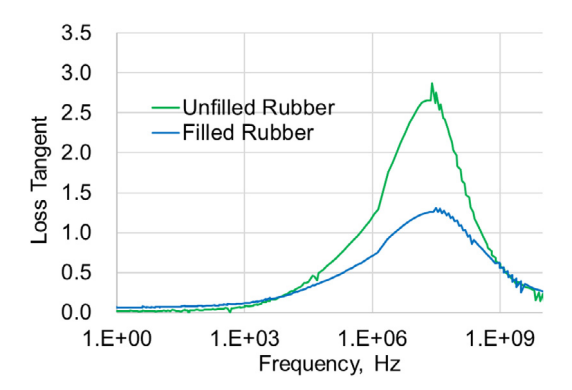


Fig. 4. Measured Loss Tangent of filled rubber. The peak of the filled rubber is less than that of unfilled rubber. The loss tangent in the low frequency region is higher than that of unfilled rubber.

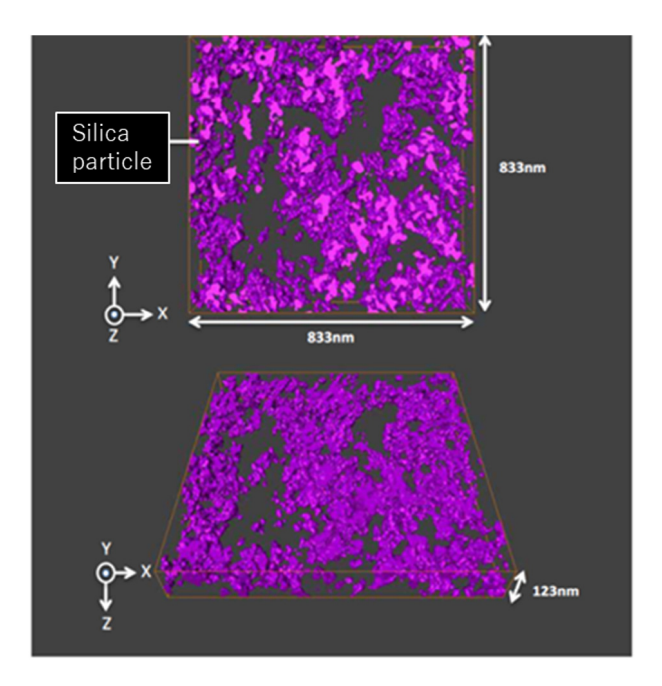


Fig. 5. 3D-image of measured filler structure in top view and in front view. Rubber matrix material is hidden.

nanoparticles as the fiducial markers. The tilt series of TEM images after the alignment were reconstructed by filtered back-projection (FBP) [19]. It took us about 2 h to take 140 TEM tilt images on TEM and a few days to align those projections before the FBP reconstruction. Each TEM image was segmented into filler and matrix phase, which takes, typically, 1 to 2 weeks. All segmented TEM images were then stacked together for the 3D image. The basic protocol used here is essentially the same as the one in which we demonstrated less than 1 nm resolution, i.e., 0.5 to 0.8 nm [25]. The reconstructed filled rubber is shown in Fig. 5.

3. Fast Fourier Transform homogenization scheme

3.1. Formulation of fast Fourier Transform scheme

3D TEM generates a high-fidelity 3D reconstruction of a filled rubber sample as a 3D digital image with a resolution of the sub-nanometer, as mentioned in the previous section. The nature of 3D TEM leads to very large structured voxel meshes making it hardly feasible for FE computation due to the fine resolution. In previous

work [6], a supercomputer was used to conduct an FE uniaxial tensile computation of the filled rubber sample. Although FE analysis is usually based on a conforming FE mesh that is adapted to the filler geometry, the authors preferred to use a non-conforming structured FE mesh directly generated from the high-resolution 3D TEM data. On the one hand, this avoided the generation of a conforming FE mesh from 3D TEM data, which is both difficult and computationally demanding. On the other hand, the non-conforming structured mesh had a large total number of degrees of freedom because it was not adapted to the filler geometry. Recent development in FFT homogenization scheme provides an alternate solution for solving boundary value problems using a non-conforming structured mesh, as mentioned in [20]. For the same non-conforming structured mesh, the FFT scheme has been shown to be much faster than the FEM [26]. Although the convergence of the FFT scheme for arbitrary phase contrasts and its efficiency can still be improved [27,28], it is a powerful homogenization scheme for 3D images. For example, the FFT scheme bypasses the need for mesh generation, which is required by the FE method, and reduces the problem size so that it can be solved on a personal computer. Although the large input image might require larger computer memory due to an increase of the total number of degrees of freedom, the FFT scheme enables a much easier approach when a high-resolution 3D digital image is provided.

In this paper, we first adopt the FFT scheme assuming small strain based on the system of equations shown in Eq. (1).

$$\begin{cases} \nabla.\sigma\left(\mathbf{X}\right) = 0, \, \forall \mathbf{X} \in \Omega_0 & \text{(equilibrium)} \\ \sigma\left(\mathbf{X}\right) = f\left(\mathbf{X}, \boldsymbol{\epsilon}\right) & \text{(constitutive law)} \\ \boldsymbol{\epsilon} = \text{sym}\left(\nabla \mathbf{u}^*\right) + \boldsymbol{\epsilon}^{\text{Macro}} & \text{(compatibility)} \end{cases} \tag{1}$$

where the applied displacement field \mathbf{u}^* is periodic over the computation domain Ω_0 . The equilibrium condition for any input mesh is given in Eq. (2):

$$\nabla \cdot \mathbf{\sigma}(\mathbf{X}) = 0, \forall \mathbf{X} \in \Omega_0$$
 (2)

In the FFT scheme, each voxel in the input image represents a material point. The location of the voxel is represented by X. Stress and strain tensors at all material points are computed in the FFT scheme. The local stress $\sigma(X)$ can be computed using any given constitutive law, but we assume linear elasticity for now.

To solve Eq. (2), the FE approach would formulate the Cauchy momentum equation with periodic boundary conditions. Here, the local strain is given as in Eq. (1). It is composed of $sym(\nabla \mathbf{u}^*)$, the symmetric part of the gradient of the periodic displacement field \mathbf{u}^* , and $\boldsymbol{\varepsilon}^{\text{Macro}}$, the prescribed macroscopic strain tensor. Introducing the polarization stress $\boldsymbol{\tau}$ and the Green's operator $\boldsymbol{\Gamma}^0$, it is possible to express to the local strain as a Lippmann–Schwinger equation:

$$\varepsilon(\mathbf{X}) = -\left(\mathbb{F}^{0} * \mathbf{\tau}\right)(\mathbf{X}) + \varepsilon^{\text{Macro}}$$
(3)

The polarization stress τ and the explicit form of the Green's operator \mathbb{F}^0 in Fourier space are defined in Eqs. (4) and (5) respectively:

$$\tau(\mathbf{X}) = \mathbb{C}^0 \colon \epsilon(\mathbf{X}) - \sigma(\mathbf{X}) \tag{4}$$

where $\mathbb{C}^{\mathbf{0}}$ is the standard stiffness tensor of an isotropic reference material, written as $C^0_{klmn} = \lambda^0 \delta_{kl} \delta_{mn} + 2\mu^0 \delta_{km} \delta_{ln}$ in index notation, with reference Lamé parameters λ^0 and μ^0 . λ^0 is computed as the algorithmic average of λ^{filler} and λ^{matrix} , and μ^0 is computed as the algorithmic average of μ^{filler} and μ^{matrix} . λ^{filler} , λ^{matrix} , μ^{filler} , and μ^{matrix} are given a priori.

$$\hat{I}_{klmn}^{0}(\xi) = \frac{\delta_{km}\xi_{l}\xi_{n}}{2\mu^{0}|\xi|^{2}} - \frac{\lambda^{0}}{2\mu^{0}(\lambda^{0} + 2\mu^{0})} \frac{\xi_{k}\xi_{l}\xi_{m}\xi_{n}}{|\xi|^{4}}$$
(5)

where the indices of $\hat{\Gamma}^0_{klmn}$ coincide with those of C^0_{klmn} .

Since the explicit form of the Green's operator is known only in Fourier space, the convolution term in Eq. (4) is computed with the help of the inverse Fourier transform as in Eq. (6).

$$\mathbb{\Gamma}^{0} * \mathbf{\tau} (\mathbf{X}) = \mathcal{F}^{-1} \left\{ \widehat{T}_{klmn}^{0} (\xi) \mathcal{F} [\tau_{kl} (\mathbf{X})] \right\}$$
(6)

where ${\cal F}$ and ${\cal F}^{-1}$ denote respectively the FFT and the inverse FFT.

To solve the above FFT formulation, various iterative methods can be used, such as fixed point iteration and conjugate gradient. The solution techniques are vastly available in the literature, such as [27,29]. For demonstration purposes, the FFT algorithm is presented using fixed point iteration in Appendix A.

The iteration process of the FFT algorithm starts from a given initial local strain and checks for convergence on the local $\varepsilon(X)$. During the iteration process, Green's function enforces the compatibility condition given in Eq. (1). To obtain the macroscopic stress and strain tensors from the mesh, volumetric average following Hill's lemma are conducted as in Eq. (7):

$$\mathbf{\sigma}^{\text{Macro}} = \frac{1}{|V|} \int_{V} \mathbf{\sigma}(\mathbf{X}) dV \text{ and } \mathbf{\epsilon}^{\text{Macro}} = \frac{1}{|V|} \int_{V} \mathbf{\epsilon}(\mathbf{X}) dV$$
 (7)

To obtain effective elastic material properties μ^{Macro} and λ^{Macro} , σ^{Macro} and $\varepsilon^{\text{Macro}}$ are plugged into Hooke's law as in Eq. (8):

$$\sigma_{ij}^{Macro} = \lambda^{Macro} \varepsilon_{kk}^{Macro} \delta_{ij} + 2\mu^{Macro} \varepsilon_{ij}^{Macro}$$
(8)

It is convenient to compute μ^{Macro} and λ^{Macro} by solving Eq. (8). One can re-write Eq. (8) in matrix format and solve for μ^{Macro} and λ^{Macro} .

3.2. Application of FFT scheme for frequency domain computation

For rubber materials or viscoelastic materials in general, responses are drastically different for various loading frequencies; DMA is a common experimental method to evaluate this variation. DMA provides viscoelastic material properties, such as the complex Young's modulus, $E^* = E' + iE''$, and the complex shear modulus, at different frequency points, denoted as ω_k . The ratio between the E'', the imaginary part of the complex Young's modulus, and E', the real part of the complex Young's modulus, gives the $\tan(\delta)$ curve. Complex shear modulus is defined as $G^* = G' + iG''$.

For DMA, a sinusoidal strain with a given frequency ω_k is applied to the rubber and the steady state stress is measured to compute viscoelastic material properties. In the 1D case, the stress at a given peak strain $\varepsilon_0^{\text{Macro}}$ can be written as:

$$\sigma^{\text{Macro}}(t) = \Re \left[\varepsilon_0^{\text{Macro}} E^* (\omega_k) e^{i\omega_k t} \right]$$

$$= \Re \left[\varepsilon_0^{\text{Macro}} (E'(\omega_k) + i E''(\omega_k)) (\cos (\omega_k t) + i \sin(\omega_k t)) \right]$$
(9)

where, for any complex number z, $\Re[z]$ is the real part of z.

A steady-state solution for σ^{Macro} (t) can be found by simply taking $t=0, \frac{2\pi}{\omega_k}, \frac{4\pi}{\omega_k}, \dots$ The steady state stress can then be treated as a complex one, written as $\sigma^{\text{Macro},*} = \varepsilon_0^{\text{Macro}}(E'(\omega_k) + iE''(\omega_k))$. $\sigma^{\text{Macro},*}$ is composed of a real part and an imaginary part. For the 1D case, taking the quotient of $\sigma^{\text{Macro},*}$ and $\varepsilon_0^{\text{Macro}}$ yields the complex Young's modulus. Reciprocally, the complex stress can be computed by the FFT scheme by inputting the complex Young's modulus.

The above operation is to be performed at a given frequency point ω_k . To compute the rubber's $\tan(\delta)$ curve, an individual $\tan(\delta)$ point at different ω_k is needed, where $\tan(\delta)$ is defined as $\tan(\delta) = \frac{E''}{E'}$ for tensile DMA and $\tan(\delta) = \frac{G''}{G'}$ for shear DMA. Therefore, by computing the rubber's responses at different frequency points, the complex Young's modulus or shear modulus can be obtained, and $\tan(\delta)$ can then be computed. When a sufficient number of ω_k is taken, a smooth $\tan(\delta)$ curve of filled rubber can be reconstructed.

In this paper, shear DMA of both unfilled and filled rubber are conducted to reconstruct master curves. However, due to the limitation of experimental conditions, only complex shear moduli at different frequencies are available. An assumption is that for a complex shear modulus, a conversion to the Lamé constants is still valid. This enables computation of $tan(\delta)$ using the FFT scheme at various frequency points for the filled rubber by inputting properties of basic constituents: unfilled rubber and fillers.

A computation using unfilled rubber complex shear moduli at different frequency points and filler properties is performed using the mesh introduced in Section 2. To make the computation more feasible, the filled rubber domain shown in Section 2 is shrunk by 1/2 in all three directions to $513 \times 513 \times 75$ voxels, where the length of each voxel's edge is 1.62 nm. Poisson's ratio of the unfilled rubber is taken as 0.499, allowing for limited compressibility of rubber materials. Note that the aforementioned assumption can be improved by choosing a frequency dependent

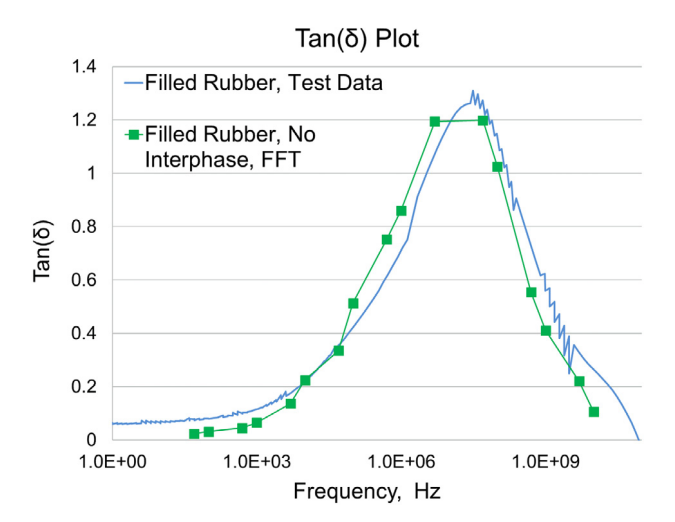


Fig. 6. $Tan(\delta)$ of filled rubber compared to experimental results.

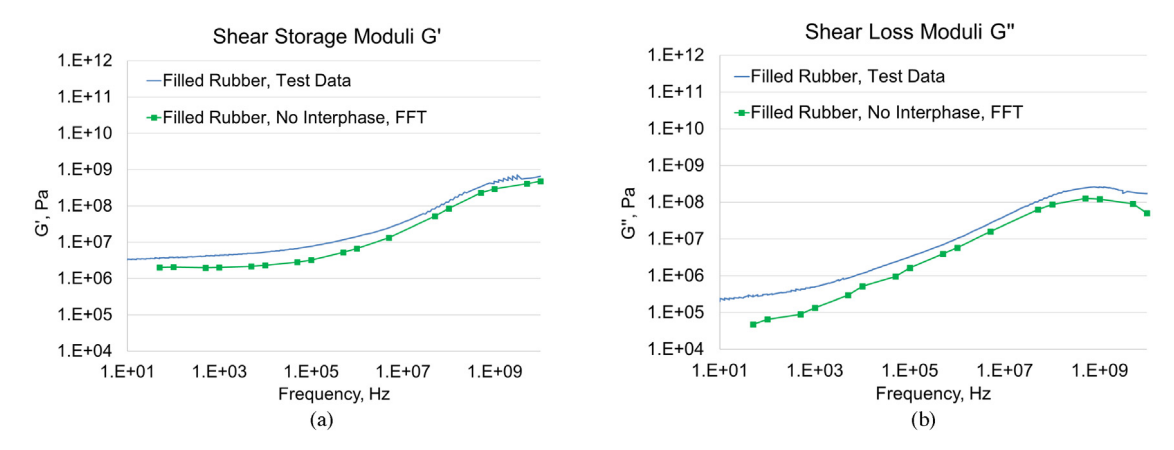


Fig. 7. (a) Shear storage moduli G' and (b) Shear loss moduli G" comparison between FFT and experimental results.

Poisson's ratio to account for limited compressibility in the glassy state, given enough experimental data from material characterization. This will be addressed in future work. The filler material has Young's modulus E=300 MPa and Poisson's ratio $\nu=0.19$. This value of Young's modulus for the filler material is chosen in order to avoid deteriorating the convergence of the FFT scheme, which is sensitive to phase contrast. As shown in Appendix B, this value is nevertheless large enough to obtain physically meaningful results. The homogenized complex shear modulus from the FFT scheme is used to compute the $\tan(\delta)$ curve. The computed $\tan(\delta)$ curve and the experimental result are shown in Fig. 6.

The results in Fig. 6 illustrate the inconsistency between prediction and experimental measurement of $\tan(\delta)$. It can be deduced from the figure that before the peak of $\tan(\delta)$, the two-phase model follows a different trend than experimental results. In the low-frequency region (less than 1e5 Hz), $\tan(\delta)$ is lower than experimental measurements. Between 1e5 Hz and 5e7 Hz, $\tan(\delta)$ is overestimated.

The predicted G' and G'' of filled rubber model are shown in Fig. 7(a) and (b). In Fig. 7(a), the prediction of G' in the low-frequency region, i.e., between 1e1 Hz and 1e5 Hz, is 50% smaller than experimental values. In the same region, shown in Fig. 7(b), the predicted loss modulus G'' can be as low as 100% below the experimental values. Such discrepancy between simulation and prediction result in lower $\tan(\delta)$ as shown in Fig. 6. In the high-frequency region, between 1e5 Hz to 1e7 Hz, the predicted storage modulus has the same 50% difference w.r.t. experimental data, but the difference between the predicted G'' and experimental data decreases, resulting in a trend of increasing G''. This explains why the predicted $\tan(\delta)$, shown in Fig. 6, between 1e5 Hz and 1e7 Hz is higher

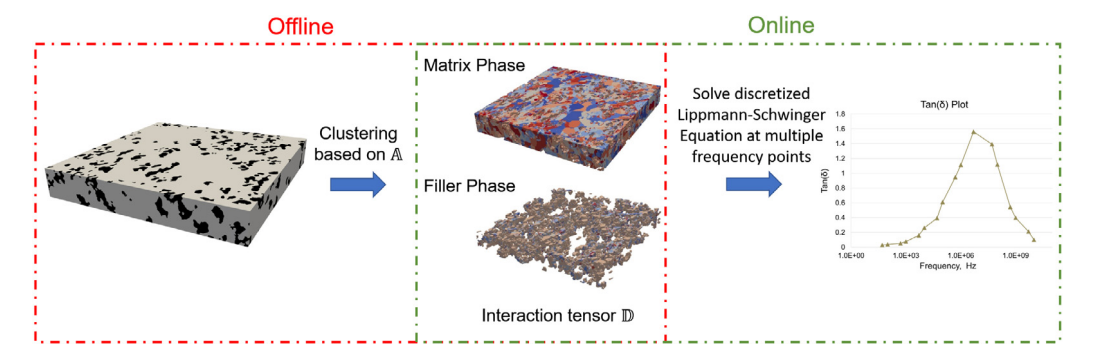


Fig. 8. Offline and online stages for filled rubber.

than the experimental data. In the region of frequency higher than 1e7 Hz, both predicted G' and G" are close to experimental results, giving a relatively good prediction of $tan(\delta)$.

Such an inconsistency observed in Fig. 6 is expected, as the input mesh only considered rubber and filler phases. As mentioned in the introduction, the existing literature supports the assumption that there is an interphase region between the filler and pure rubber that should be treated as a third material. Specifically, the interphase should have a larger G" compared to unfilled rubber in the lower frequency region between 1e1 Hz and 1e5 Hz. It should also have a larger G' compared to the unfilled rubber in the frequency region between 1e5 Hz and 1e7 Hz. The original two-phase model is incomplete and cannot fully reveal the property of filled rubber, which would be required to model the interphase based on the filled rubber 3D image reconstructed in Section 2. One problem that emerges after modeling the interphase in the original filled rubber mesh is that the property of the interphase stays unknown. Due to a limitation of experimental techniques, the viscoelastic property of the interphase, or its complex Young's or shear modulus, cannot be given as a known input. Therefore, we propose an inverse modeling technique to compute the interphase property quantitatively, described in the next section, with the aim of producing a better prediction of $tan(\delta)$ of filled rubber. However, the inverse modeling procedure requires multiple iterations, and the FFT procedure has to be performed in all iterations. This will impose a considerable computational cost. To address the computational efficiency issue, a reduced order modeling approach is also introduced to reduce the computational cost of evaluating filled rubber responses at each frequency point. The reduced order modeling approach is then combined with the inverse modeling procedure to compute interphase properties and filled rubber properties.

4. Efficient reduced order modeling for the filled rubber composite

The aforementioned FFT formulation can compute the effective property of filled rubber, but it requires the computation of all local responses at individual voxels and thus imposes a high computational cost. The recently proposed SCA method [30–32] provides an alternative for computing effective properties of arbitrary microstructure, such as the filled rubber composite, at a reasonable computational cost. In this section, the SCA formulation is discussed, providing insight into the physically-based reduced order model.

SCA is a two-stage reduced-order modeling approach. In the offline stage, two steps are performed: (1) all voxel elements in the mesh are clustered based on an arbitrary measurement for similarity in mechanical responses, such as the strain concentration tensor \mathbb{A} ; (2) The interaction tensor, \mathbb{D} , for each pair of clusters is then computed. The offline stage will generate a material microstructure database which contains all interaction tensors between clusters pairs and volume fraction of each cluster. After the offline stage, the original high fidelity RVE is compressed into a small number of clusters. In the online stage, discretized Lippmann–Schwinger will compute strain and complex stress in each clusters and RVE level averaged complex stress and strain at any given external loading conditions by solving a boundary value problem. Once the RVE complex stress is identified, $\tan(\delta)$ will be computed accordingly. This process is concisely illustrated in Fig. 8. Note that in the previous section, RVE complex stress at each frequency point is computed by FFT. Here, voxels are assumed to be "once responded same, always responds the same". Therefore, the offline database can be constructed once. The database can be used for all frequency points afterward for an efficient evaluation of $\tan(\delta)$ at different frequency points.

The Lippmann-Schwinger equation given in Eq. (3) can be reformulated in the following form in Eq. (10)

$$\mathbf{\varepsilon}^{\text{Macro}} - \mathbf{\varepsilon} \left(\mathbf{X} \right) - \int_{\Omega} \mathbb{F}^{\mathbf{0}} \left(\mathbf{X}, \mathbf{X}' \right) : \left[\mathbf{\sigma} \left(\mathbf{X}' \right) - \mathbb{C}^{0} : \mathbf{\varepsilon} \left(\mathbf{X}' \right) \right] d\mathbf{X}' = 0, \ \mathbf{X} \in \Omega$$
(10)

where X is the voxel element location in the mesh and X' is the location in the reference domain.

To perform reduced order modeling of the filled rubber composite, one can reduce overall degrees of freedom in the mesh by grouping voxels with similar mechanical responses together. This process is also known as clustering. A convenient criterion chosen here is the well-known strain concentration tensor \mathbb{A} that connects macroscopic prescribed strain to local strain responses at each voxel, shown in Eq. (11):

$$\mathbf{\varepsilon}(\mathbf{X}) = \mathbb{A}(\mathbf{X}) : \mathbf{\varepsilon}^{\text{Macro}}, \ \mathbf{X} \in \Omega$$
 (11)

where \mathbb{A} is a 6 by 6 matrix in Voigt notation. Six traction free loadings on the original RVE are needed in order to determine all 36 entries of \mathbb{A} [30]. Clustering algorithms, such as k-means clustering, can be used to cluster all voxels and decompose the original domain of 19,737,675 voxels into K clusters, where K equals 64. This is the first step of the offline stage. One might think of this as reducing the total integration points to K, where K is a small number compared to the total number of integration points in the original mesh. Note that \mathbb{A} is not the sole solution for the clustering process. For different problems, one might wish to use other meaningful quantities to identity voxels with similar mechanical responses, such as lattice orientation [31].

It is convenient to define a characteristic function as in Eq. (12) in order to decompose Eq. (10) to incorporate the newly decomposed domain.

$$\chi^{I}(\mathbf{X}) = \begin{cases} 1 & \mathbf{X} \in \Omega^{I} \\ 0 & \text{otherwise} \end{cases}$$
 (12)

where I = 1, 2, 3, ..., K. The discretized Lippmann–Schwinger equation is given in Eq. (13) for each cluster.

$$\epsilon^{\text{Macro}} - \frac{1}{c^{\text{I}} |\Omega|} \int_{\Omega} \chi^{\text{I}}(\mathbf{X}) \, \mathbf{\epsilon}(\mathbf{X}) \, d\mathbf{X}
- \frac{1}{c^{\text{I}} |\Omega|} \int_{\Omega} \int_{\Omega} \chi^{\text{I}}(\mathbf{X}) \, \mathbb{F}^{\mathbf{0}}(\mathbf{X}, \mathbf{X}') \colon [\mathbf{\sigma}(\mathbf{X}') - \mathbb{C}^{0} \colon \mathbf{\epsilon}(\mathbf{X}')] d\mathbf{X}' d\mathbf{X}
= 0, \mathbf{X} \in \Omega$$
(13)

where c^{I} is the volume fraction of cluster I and $|\Omega|$ is the total volume of the mesh.

By noticing that $\sigma(X')$ and $\varepsilon(X')$ can be written as:

$$\sigma(\mathbf{X}') = \sum_{J=1}^{K} \chi^{J}(\mathbf{X}') \, \sigma^{J}, \ \varepsilon(\mathbf{X}') = \sum_{J=1}^{K} \chi^{J}(\mathbf{X}') \, \varepsilon^{J}$$
(14)

Now Eq. (13) becomes:

$$\epsilon^{\text{Macro}} - \frac{1}{c^{\text{I}} |\Omega|} \int_{\Omega} \chi^{\text{I}}(\mathbf{X}) \, \epsilon(\mathbf{X}) \, d\mathbf{X}
- \frac{1}{c^{\text{I}} |\Omega|} \sum_{J=1}^{K} \int_{\Omega} \int_{\Omega} \chi^{\text{I}}(\mathbf{X}') \chi^{J}(\mathbf{X}') \mathbb{F}^{\mathbf{0}}(\mathbf{X}, \mathbf{X}') \colon \left[\mathbf{\sigma}(\mathbf{X}') \right.
\left. - \mathbb{C}^{0} \colon \epsilon(\mathbf{X}') \right] d\mathbf{X}' d\mathbf{X} = \mathbf{0}, \ \mathbf{X} \in \Omega$$
(15)

where \mathbb{D}^{IJ} is:

$$\mathbb{D}^{IJ} = \frac{1}{c^{I} |\Omega|} \int_{\Omega} \int_{\Omega} \chi^{I}(\mathbf{X}) \chi^{J}(\mathbf{X}') \mathbb{F}^{\mathbf{0}}(\mathbf{X}, \mathbf{X}'), \ \mathbf{X} \in \Omega$$
 (16)

After the first step of the offline stage process, which is the clustering process, \mathbb{D}^{IJ} can be computed. Once \mathbb{D}^{IJ} is computed, the second step of the clustering process is completed, and the original RVE is compressed into a microstructural database made of clusters and interaction tensors. Plugging in \mathbb{D}^{IJ} into Eq. (13) will give the final

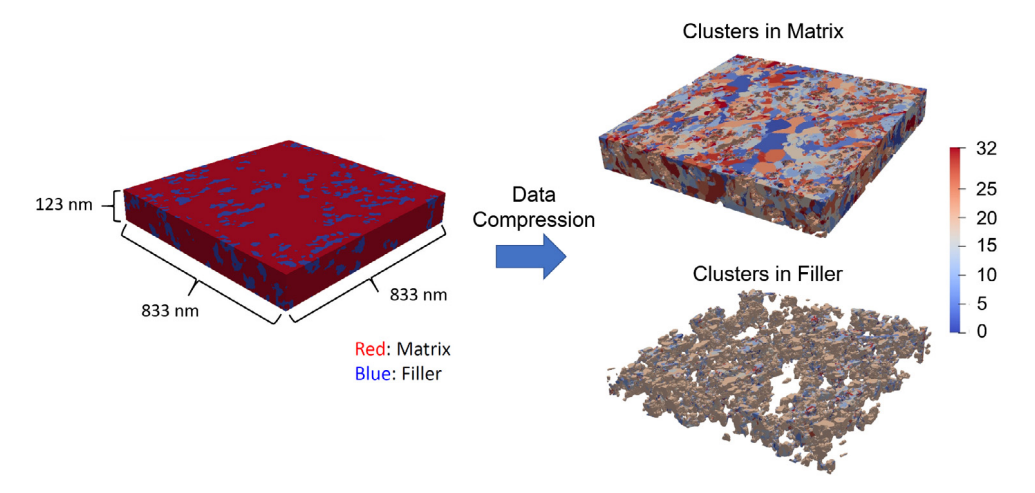


Fig. 9. Clusters of filled rubber in matrix phase and filler phase.

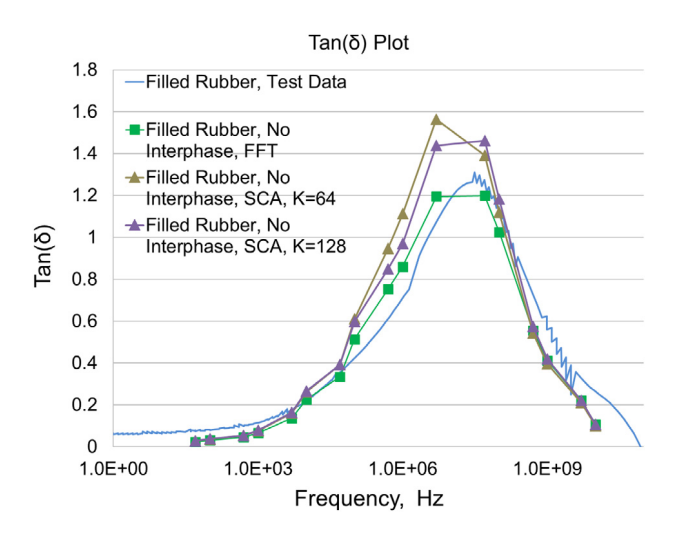


Fig. 10. $Tan(\delta)$ of filled rubber computed by SCA.

form of the discretized Lippmann-Schwinger equation in Eq. (17):

$$\boldsymbol{\epsilon}^{\text{Macro}} - \boldsymbol{\epsilon}^{\text{I}} - \sum_{J=1}^{K} \mathbb{D}^{\text{IJ}} \colon \left[\boldsymbol{\sigma}^{J} - \mathbb{C}^{0} \colon \boldsymbol{\epsilon}^{J} \right] = \boldsymbol{0}, \text{I} = 1, 2, 3, \dots, K$$
 (17)

where the incremental form is given as:

$$\Delta \boldsymbol{\varepsilon}^{\text{Macro}} - \Delta \boldsymbol{\varepsilon}^{\text{I}} - \sum_{J=1}^{K} \mathbb{D}^{\text{IJ}} \colon \left[\Delta \boldsymbol{\sigma}^{\text{J}} - \mathbb{C}^{0} \colon \Delta \boldsymbol{\varepsilon}^{\text{J}} \right] = \boldsymbol{0}, \ \text{I} = 1, 2, 3, \dots, K$$
 (18)

The online stage involves the evaluation process of Eq. (18). The solution procedure of Eq. (18) is given in Appendix C for readers' reference.

The above SCA formulation is combined with Eq. (9) to compute the effective complex moduli of filled rubber at a reduced computational cost due to the reduction of the number of integration points and degrees of freedom. The Reduced Order Model (ROM) of the original filled rubber domain with clusters is shown in Fig. 9 for 32 clusters per phase. A second ROM with 64 clusters per phase (making 128 clusters in total) is also generated but not shown for the sake of space. The corresponding master curve is given in Fig. 10, where the comparison with the FFT result is shown. The master curves computed by the ROM show a trend of the overall effective filled rubber

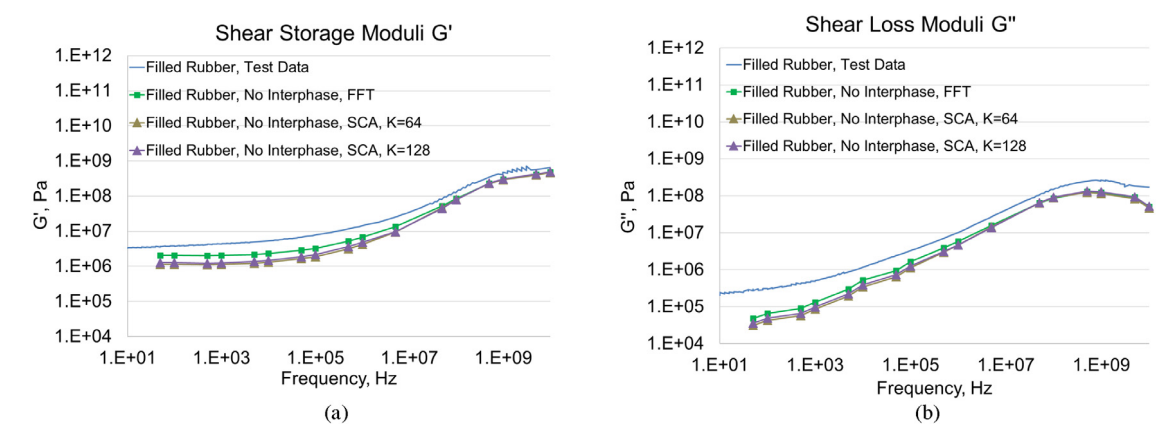


Fig. 11. (a) Shear storage moduli G' plots and (b) Shear loss moduli G' plots.

Table 2Comparison of computation time over 17 frequency points.

	Computation time
FFT	4023 s per frequency point,
	68,400 s total CPU time
ROM (64 clusters)	Offline:
	7 h (strain concentration
	tensor generation)
	5 h (clustering + interaction
	tensor generation)
	Online:
	4.35 s per frequency point,
	74 s total CPU time

performance that is consistent with the results computed by the FFT algorithm. Although SCA overestimates the $\tan(\delta)$ curve, the results were obtained with a dramatic reduction of computation time with a speedup of 924 at 64 clusters (32 clusters in the filler phase and 32 clusters in the unfilled rubber phase). The comparison between computation time using SCA and FFT are shown in Table 2. In Fig. 11, the filled rubber G' and G'' computed by SCA are in the same trend. However, SCA provides considerable savings in terms of computation time. The difference between FFT and SCA predictions are within one order of magnitude. This means the ROM does not sacrifice all microstructure information after the clustering process. Both FFT and SCA predict the same trend of filled rubber G' and G'', meaning that the deviation caused by the interphase needs to be captured as mentioned in the previous section.

To further investigate interphase properties using our reduced order model approach, the above procedure is integrated into the inverse modeling process to better predict filled rubber properties.

5. Inverse modeling scheme for the interphase

With the master curves shown in Fig. 10, it is clear that a two-phase filled rubber model is not sufficient in representing the true filled rubber behavior. The cause of this inconsistency between computed $\tan(\delta)$ curves and experimental measurement can be attributed to the interphase region between the filler material and unfilled rubber. Therefore, in the following discussion, the presence of the interphase between filler and matrix materials is considered. This should reduce the difference between the $\tan(\delta)$ curves plotted in Fig. 10. The interphase is assumed to surround the filler in a spherical region with a radius β_{IP} of 9.74 nm. Note here that the interphase is assumed to be uniform, meaning its thickness is constant throughout the whole domain. A voxel-wise search of the filled rubber 3D-image shown in Section 2 is performed to convert the elements within β_{IP} from the matrix to the interphase.

5.1. Inverse modeling formulation

The filled rubber model with the interphase can be created following the aforementioned voxel-wise search process, but the viscoelastic behavior of interphase is still unknown. The interphase is used to suppress the inconsistency between master curves from the FFT homogenization scheme and experimental data, thus its complex Young's or shear moduli at different ω_k have to be computed. To predict the unknown interphase property with limited experimental data, a so-called inverse modeling scheme is introduced based on optimization techniques. The objective function of the inverse modeling process can be written as:

$$G^{*, \text{IP}}(\omega_{k}) = \underset{G^{*, \text{IP}}(\omega_{k}) = G', \text{ IP}(\omega_{k}) + iG'', \text{ IP}(\omega_{k})}{\text{arg min}} \quad \text{norm} \left[\left(G'^{, \text{PMC}} \left(\widetilde{G^{*, \text{IP}}}(\omega_{k}), \omega_{k} \right) - G'^{, \text{EXP}}(\omega_{k}) \right) + i \left(G''^{, \text{PMC}} \left(\widetilde{G^{*, \text{IP}}}(\omega_{k}), \omega_{k} \right) - G''^{, \text{EXP}}(\omega_{k}) \right) \right]$$

$$(19)$$

Above goal function states for each given ω_k , the solution of interphase complex shear modulus $G^{*,PMC}$ (ω_k) is found when the difference of predicted complex shear modulus $G^{*,PMC}$ ($G^{*,PMC}$, ω_k) and $G^{*,EXP}$ (ω_k) is minimized. When ω_k is fixed, it is possible to define a function for the root-finding process as:

$$f(G^{*,IP}) = G^{*,PMC}(G^{*,IP}) - G^{*,EXP}$$
(20)

where ω_k is omitted compared to Eq. (10) since the solution is found for each ω_k of interest.

To solve for Eq. (20), an iterative method is used to find the solution of $G^{*,IP}(\omega_k)$. The derivative of Eq. (20) can be formulated as in Eq. (21) in order to apply Newton's iterative method:

$$f'(G^{*,IP}) = \frac{(G^{*,PMC,^{n}} - G^{*,EXP}) - (G^{*,PMC^{n-1}} - G^{*,EXP})}{G^{*,IP^{n}} - G^{*,IP^{n-1}}}$$
(21)

With Eqs. (20) and (21), it is possible to write the iterative process as Eq. (22):

$$G^{*,IP^{n+1}} = G^{*,IP^n} - \frac{G^{*,PMC^n} - G^{*,EXP}}{\left[\frac{(G^{*,PMC^n} - G^{*,EXP}) - (G^{*,PMC^{n-1}} - G^{*,EXP})}{G^{*,IP^n} - G^{*,IP^{n-1}}}\right]}$$
(22)

where the superscript n denotes the current iteration number and n+1 denotes the next iteration. The initial guess for interphase properties is set to be the same as an unfilled rubber.

5.2. Inverse modeling for the filled rubber model with interphase

The proposed inverse modeling method is applied to the aforementioned filled rubber domain to re-compute the filled rubber master curve. The mesh is the one used in Section 3.2, but with the added interphase. An interphase of thickness $\beta^{IP} = 9.74$ nm, which is equivalent to 6 voxels, is added to the domain to create the filled rubber model with the interphase. The updated filled rubber mesh with the interphase is shown on the left of Fig. 12. The corresponding ROM of the above three-phase model has also been constructed and shown on the right of Fig. 12. Fig. 12 shows the ROM with 32 clusters in each phase, meaning the whole filled rubber mesh is compressed into 96 clusters.

For the inverse modeling process, 17 frequency points are picked over the span of the entire master curve of filled rubber. More points can be used for the inverse modeling process but would increase computational cost. The experimental procedure of measuring the filled and unfilled rubber master curves have been reported in Section 2. Material properties for unfilled rubber and filler materials are those introduced in Section 3.2. The inverse modeling process is combined with the SCA online prediction to be the third step of the present scheme. At this point, the three-step prediction scheme for filled rubber is presented. The results of the inverse modeling will be presented and discussed in the next section.

6. Result and discussion on inverse modeling results

In this section, the numerical prediction of the filled rubber properties are presented. Through inverse modeling, a more accurate prediction of the filled rubber master curve is shown in Fig. 13. Predicted $tan(\delta)$ curves by both the FFT and SCA method are a good match with measured experimental data. The SCA result is consistent with

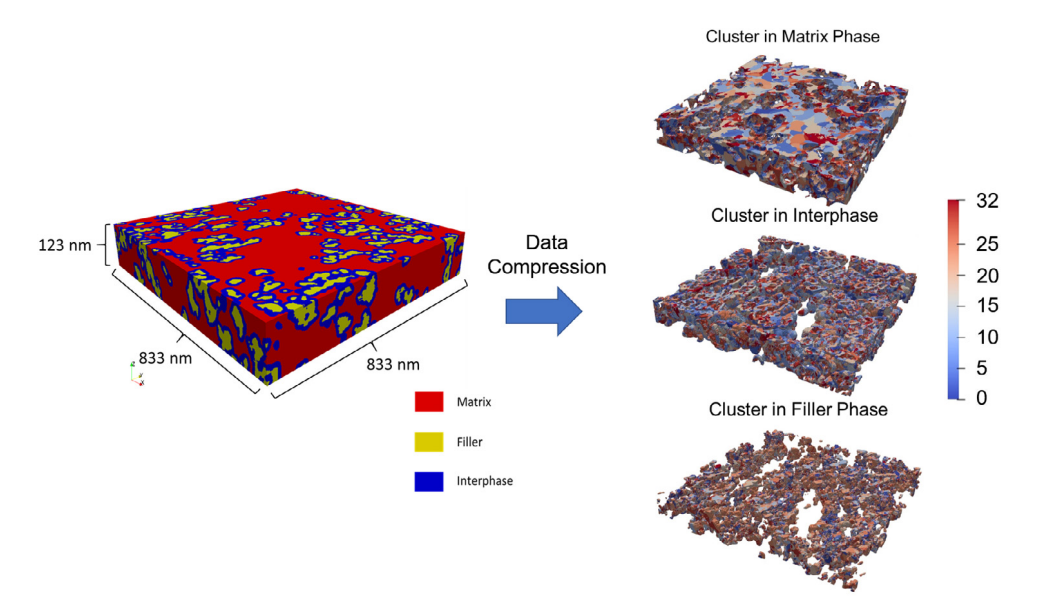


Fig. 12. Filled rubber with an interphase of 9.74 nm and clusters of filled rubber in matrix phase, filler phase, and interphase.

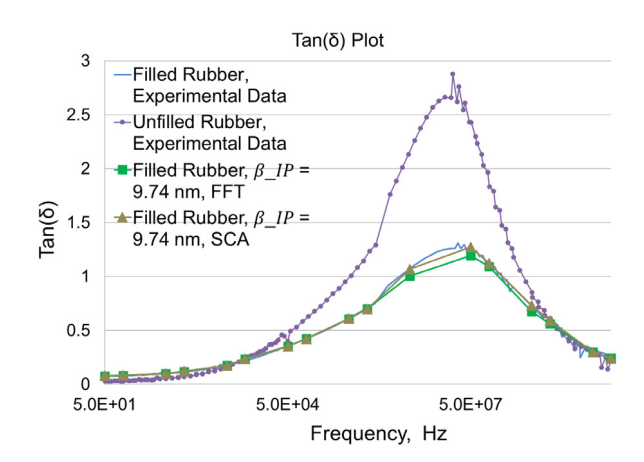


Fig. 13. Predicted master curve of filled rubber by FFT and SCA vs. experimental results.

the FFT result, meaning the current ROM provides sufficient accuracy in predicting overall behavior of the filled rubber.

The comparison between the predicted G' and G" of the filled rubber and experimental results are shown in Fig. 14(a) and (b), respectively. It can be concluded that with the consideration of the interphase, the prediction of $tan(\delta)$ is a good match with the experimental data.

Through inverse modeling, G' and G" of interphase are computed as well, as shown in Fig. 14(a) and (b). As stated in Section 4, the interphase should have larger G' and larger G" compared to unfilled rubber properties. Only then the filled rubber G' and G" can be improved and match with experimental results. The inverse modeled interphase properties ensure the prediction of the filled rubber's behavior follows the experimental data. It is worth noting the interphase G' and G" predicted by the ROM through SCA is higher than that obtained from FFT, but both SCA and FFT predict the same trend of the filled rubber G' and G" as a function of frequency. Such a deviation is expected since the G' and G" predicted using a 2-phase filled rubber by SCA are smaller than predictions made by FFT. Higher interphase G' and G" will offset such differences in order to comply with the objective function defined in Eq. (19).

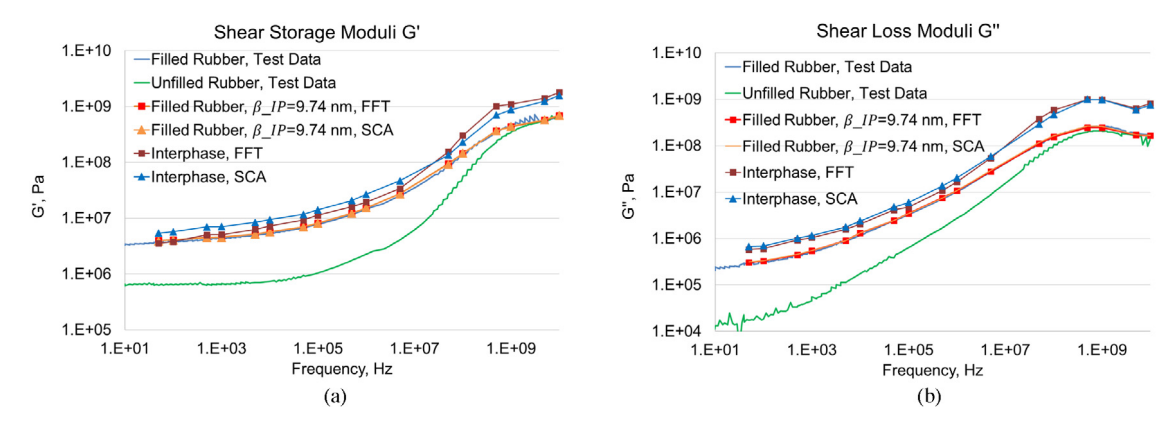


Fig. 14. (a) Predicted G' and (b) Predicted G" of filled rubber vs. experimental results.

Table 3Comparison of inverse modeling CPU time at single frequency point.

	Computational CPU time
FFT	~35,576 s
ROM (96 clusters)	20 s

The difference observed between the filled rubber and unfilled rubber $tan(\delta)$ shown in Fig. 13 suggests that the filled rubber would have less rolling resistance due to smaller $tan(\delta)$ measured at a lower frequency range (1e4 Hz and 1e6 Hz). It is possible to link such characteristics to computed interphase properties, in which higher storage and loss moduli are observed, shown in Fig. 14. This leads to a lower $tan(\delta)$ of the interphase, leading to a decreased overall hysteresis of the filled rubber by reducing filled rubber $tan(\delta)$. Hence, the filled rubber would have less rolling resistance compared to the pure rubber. In the same figure, it can be concluded that both SCA and FFT capture the glass transition region, signified by the peak of $tan(\delta)$ curves.

On the other hand, Fig. 13 shows little difference between the filled and unfilled rubber $\tan(\delta)$ in the high-frequency range. This suggests that in the high-frequency range both materials should behave in a similar fashion. The computed interphase storage and loss moduli do not vary much from the unfilled rubber properties as shown above. Therefore, the computed interphase properties are consistent with measured $\tan(\delta)$ of the filled rubber compound.

Also, the peak $tan(\delta)$ of the filled rubber is lower than unfilled rubber. In order to increase tire traction at low temperatures, $tan(\delta)$ at lower temperatures should be increased. Based on the computed filled rubber properties, this can be achieved by identifying filler material that can form interphase with high loss modulus in the high-frequency range. Such a material combination would provide increased damping so the winter traction can be improved. The present workflow is suitable to inversely model necessary interphase storage and loss moduli that narrow down the domain for material selection.

In addition, a dramatic increase in computational efficiency was observed for the SCA prediction. The comparison of the computation time of inverse modeling at a single frequency point is shown in Table 3, where a 1778 speed-up is achieved by applying the proposed ROM compared to FFT. A comparison of computational time in evaluating filled rubber properties by different methods is summarized in Table 4. SCA requires an offline stage computation to generate the ROM of the filled rubber composite, which can be computationally expensive. However, once the database is computed, it can be used for all later evaluations. This provides considerable savings in computational time in the online stage prediction of effective properties of the filled rubber, as well as the inverse modeling process. The SCA method, combined with inverse modeling, opens a new avenue towards material design. Moreover, the same sets of ROM can be used for various material properties to compute filled rubber mechanical behaviors at a reasonable cost. It is possible to explore the design space and get both a decent trend and quantitative description of filled rubber. More importantly, the proposed scheme provides an efficient solution towards investigating interphase properties of filled rubber materials for future design needs, even with limited computational resource.

Method	Degrees of freedom (count)	Memory required	Computation time
FEM	200 million	1 TB	1 million hr. CPU time (with 6144 cores on a supercomputer)
FFT	118 million	53 GB	9.88 h. per frequency point, 168 h. CPU time (5,952 speed-up)
118 m	Offline: 118 million Online:	Offline: 53 GB Online:	Offline: 19 h 11 h (strain concentration tensor generation) 8 h (clustering + interaction tensor
	576	less than 1 GB	generation) Online Prediction: 20 s per frequency point, 340 s CPU time (52.631 speed-up)

Table 4Speed comparison of filled rubber property evaluation for a model of size 513×513×75 using different methods ¹

Despite the encouraging results observed using the inverse modeling scheme, necessary assumptions were made for this process to be possible. For example, the interphase thickness β^{IP} was assumed to be in a circular region around the filler material. However, it is possible for the interphase thickness to be a function of the filler curvature or filler size since the degree of polymer chain aggregation can be affected by such parameters. The scheme will be extended to include varying interphase thickness around the filler to consider this geometrical effect.

7. Conclusion

In this manuscript, an inverse modeling scheme is introduced and illustrated as an effort of quantitatively analyzing the interphase properties of a filled rubber compound using high fidelity reconstruction of the filled rubber sample. The FFT scheme enables efficient computation when a fine 3D digital image is used as input, and the future work will address further development of the method to handle a 3D image that is not naturally periodic. The test data of unfilled and filled rubber provide enough inputs to solve an inverse modeling process for interphase properties at each frequency point. In addition, SCA, a reduced order modeling scheme, is combined with the inverse modeling procedure to compute interphase properties for the first time. Once the offline stage database is constructed, the database can be conveniently used at all frequency points to compute the whole filled rubber master curve. This novel reduced order modeling approach provides considerable savings in terms of computational cost. The consolidation of SCA and the inverse modeling scheme is an efficient and valuable filled rubber design tool. The present method is general enough and can incorporate other details of the microstructure, such as variation of interphase thickness. The obtained interphase property can enable forward computation of a three-phase filled rubber model in the time domain analysis, such as tensile testing. It is believed that the effect of interphase can yield better predictions of filled rubber responses under various loading conditions, and it shall be addressed in future work.

Acknowledgments

Jiaying Gao, Modesar Shakoor, and Wing Kam Liu gratefully acknowledge the partial support of the Bridgestone Corporation. Wing Kam Liu acknowledged the partial supported by National Science Foundation grant CMMI-1762035. The authors also greatly acknowledge the contribution of Dr. Takeshi Higuchi and Mr. Masatoshi Hirata in the experimental part of this study. This study was partially supported by Japan Society for the Promotion of Science KAKENHI, Japan (Grant No. 16H02288).

 $^{^{1}}$ Note that FEM simulation is conducted using super computer with mesh resolution of $850 \times 850 \times 91$. In FFT and SCA, a mesh resolution with $513 \times 513 \times 75$ is used due to restriction on computer memory. Nonetheless, FFT and SCA provides significant reduction on memory required and computational time

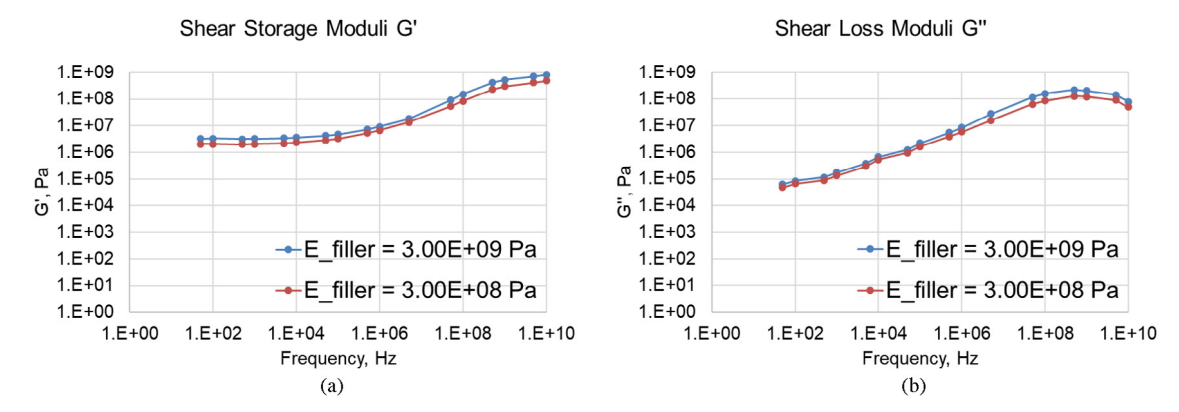


Fig. B.1. (a) G' of the filled rubber; (b) G'' of the filled rubber. The filler moduli do not affect filled rubber storage and loss moduli significantly.

Appendix A. FFT scheme algorithm flow chart

The algorithm flow chart for the FFT scheme with fixed point iteration is concisely given as below. The convergence test is used to determine if the local strain ε^{i+1} reached a stable value or not. The implementation can be easily done in any programming language, provided that FFT and inverse FFT packages are readily available. Initialization:

•
$$\boldsymbol{\epsilon}^{0}(\mathbf{X}) = \boldsymbol{\epsilon}^{Macro}, \forall \mathbf{X} \in V$$

• $\boldsymbol{\sigma}^{0}(\mathbf{X}) = \mathbb{C}(\mathbf{X}) : \boldsymbol{\epsilon}^{0}(\mathbf{X}), \forall \mathbf{X} \in V$

Iterate i+1 with $\mathbf{\varepsilon}^{i}$ and $\mathbf{\sigma}^{i}$ known

(a)
$$\widehat{\boldsymbol{\sigma}}^{i} = \mathcal{F}(\boldsymbol{\sigma}^{i})$$

(b) Convergence test
(c)
$$\begin{cases} \widehat{\boldsymbol{\epsilon}}^{i+1}(\boldsymbol{\xi}) = & \widehat{\boldsymbol{\epsilon}}^{i}(\boldsymbol{\xi}) - \widehat{\mathbb{F}}^{0}(\boldsymbol{\xi}) : \widehat{\boldsymbol{\sigma}}^{i}, \forall \ \boldsymbol{\xi} \neq 0 \\ & \widehat{\boldsymbol{\epsilon}}^{i+1}(0) = \boldsymbol{\epsilon}^{Macro} \end{cases}$$
(d) $\boldsymbol{\epsilon}^{i+1} = \mathcal{F}^{-1}(\widehat{\boldsymbol{\epsilon}}^{i+1})$
(e) $\boldsymbol{\sigma}^{i+1}(\mathbf{X}) = \mathbb{C}(\mathbf{X}) : \boldsymbol{\epsilon}^{i+1}(\mathbf{x})$

Above algorithm flow chart is for single loading step. Readers can easily modify it to multiple loading steps by defining multiple $\varepsilon^{\text{Macro}}$ for multiple loading steps.

Appendix B. Sensitivity of the filled rubber properties to filler moduli

Comparisons of G' and G'' of the filled rubber at different filler moduli are given in Fig. B.1(a) and (b), respectively

Appendix C. Self-consistent clustering online analysis solution procedure

SCA requires solving the discretized Lippmann–Schwinger equation based on external loading condition, either the fixed strain increment $\Delta \varepsilon^{\text{Macro}}$ or the fixed stress increment $\Delta \sigma^{\text{Macro}}$. The discretized Lippmann–Schwinger equation is shown as in

$$\Delta \boldsymbol{\varepsilon}^{\text{Macro}} - \Delta \boldsymbol{\varepsilon}^{\text{I}} - \sum_{J=1}^{K} \mathbb{D}^{\text{IJ}} : \left[\Delta \boldsymbol{\sigma}^{\text{J}} - \mathbb{C}^{0} : \Delta \boldsymbol{\varepsilon}^{\text{J}} \right] = 0, \text{ I} = 1, 2, 3, \dots, K$$
 (C.1)

The solution to Eq. (C.1) would be strain tensor ε^I in each cluster. In order to use Newton's Raphson method to find a solution to Eq. (C.1), the residual form is given as in Eq. (C.2)

$$\mathbf{r}^{I} = -\Delta \boldsymbol{\varepsilon}^{Macro} + \Delta \boldsymbol{\varepsilon}^{I} + \sum_{J=1}^{K} \mathbb{D}^{IJ} : \left[\Delta \boldsymbol{\sigma}^{J} - \mathbb{C}^{0} : \Delta \boldsymbol{\varepsilon}^{J} \right], I = 1, 2, 3, \dots, K$$
 (C.2)

For macro strain boundary condition, the residual of macroscopic strain is written as

$$\mathbf{r}^{K+1} = -\Delta \mathbf{\epsilon}^{\text{Macro}} + \sum_{I=1}^{K} c^{I} \Delta \mathbf{\epsilon}^{I}, I = 1, 2, 3, \dots, K$$
(C.3)

For macro stress boundary condition, the residual becomes

$$\mathbf{r}^{K+1} = -\Delta \sigma^{\text{Macro}} + \sum_{I=1}^{K} c^{I} \Delta \sigma^{I}, I = 1, 2, 3, \dots, K$$
 (C.4)

Solving for $\Delta \mathbf{\epsilon}^{I}$ by minimizing residual \mathbf{r}^{I} . Linearizing \mathbf{r}^{I} with respect to $\Delta \mathbf{\epsilon}$ yields

$$0 = \mathbf{r}^{I} + \frac{\partial \mathbf{r}^{I}}{\partial \Delta \boldsymbol{\epsilon}^{J}} \delta \boldsymbol{\epsilon}^{I}, I = J = 1, 2, 3, \dots, k, k + 1$$
 (C.5)

where Jacobian Matrix $\mathbb{M}^{IJ}=\frac{\partial \mathbf{r}^I}{\partial \varDelta \mathbf{r}^J}$ is

$$\mathbb{M}^{IJ} = \delta_{IJ}\mathbb{I} + \mathbb{D}^{IJ} \colon (\mathbb{C}^{J}_{alg} - \mathbb{C}^{0}), I = J = 1, 2, 3, \dots, k \tag{C.6}$$

For macroscopic strain boundary condition, one has:

$$\mathbb{M}^{I(k+1)} = -\mathbb{I}, \, \mathbb{M}^{(k+1)I} = c^{I}\mathbb{I}, \, \text{and} \, \mathbb{M}^{(k+1)(k+1)} = \mathbf{0}, \, I = 1, 2, 3, \dots, k$$
 (C.7)

For macroscopic stress boundary condition, one has:

$$\mathbb{M}^{I(k+1)} = -\mathbb{I}, \mathbb{M}^{(k+1)I} = c^{I}\mathbb{C}^{I}_{alo}, \text{ and } \mathbb{M}^{(k+1)(k+1)} = \mathbf{0}, I = 1, 2, 3, \dots, k$$
 (C.8)

Solving Eq. (C.5) gives $\delta \mathbf{\epsilon}^{I}$ that updates all local strain increment $\Delta \mathbf{\epsilon}^{I}$. This process should be repeated until residuals in all clusters are minimized.

References

- [1] Z. Li, H. Yu, B. Jiang, M. Poldneff, C. Burkhart, W.K. Liu, Q.J. Wang, Interfacial properties of carbon-rubber interfaces investigated via indentation pull-out tests and the JKR theory, Tribol. Lett. 52 (2013) 155–161, http://dx.doi.org/10.1007/s11249-013-0202-2.
- [2] X. Cheng, K.W. Putz, C.D. Wood, L.C. Brinson, Characterization of local elastic modulus in confi ned polymer films via AFM indentation, Macromol. Rapid Commun. 36 (2015) 391–397, http://dx.doi.org/10.1002/marc.201400487.
- [3] H. Yu, Z. Li, B. Jiang, M. Poldneff, C. Burkhart, W.K. Liu, Q.J. Wang, Determination of the viscoelastic interfacial properties between silica and SNR-based materials via a semi-empirical approach, Mech. Mater. 80 (2015) 1–12, http://dx.doi.org/10.1016/j.mechmat.2014. 09.005.
- [4] B.C. Abberton, W.K. Liu, S. Keten, Anisotropy of shear relaxation in confined thin films of unentangled polymer melts, Macromolecules 48 (2015) 7631–7639, http://dx.doi.org/10.1021/acs.macromol.5b01204.
- [5] P. Mélé, S. Marceau, D. Brown, Y. De Puydt, N.D. Albérola, Reinforcement effects in fractal-structure-filled rubber, Polymer 43 (2002) 5577–5586, http://dx.doi.org/10.1016/S0032-3861(02)00385-3.
- [6] H. Kadowaki, G. Hashimoto, H. Okuda, T. Higuchi, H. Jinnai, E. Seta, T. Saguchi, Evaluation of the appropriate size of the finite element representative volume for filled rubber composite analyses, 2016, http://dx.doi.org/10.1299/mej.16-00372.
- [7] J. Diani, P. Gilormini, Y. Merckel, F. Vion-Loisel, Micromechanical modeling of the linear viscoelasticity of carbon-black filled styrene butadiene rubbers: The role of the filler-rubber interphase, Mech. Mater. 59 (2013) 65–72, http://dx.doi.org/10.1016/j.mechmat.2012. 12.007.
- [8] M.-J. Wang, Effect of Polymer-filler and filler-filler interactions on dynamic properties of filled Vulcanizates, Rubber Chem. Technol. 71 (1998) 520–589, http://dx.doi.org/10.5254/1.3538492.
- [9] C.D. Wood, L. Chen, C. Burkhart, K.W. Putz, J.M. Torkelson, L.C. Brinson, Measuring interphase stiffening effects in styrene-based polymeric thin films, Polymer 75 (2015) 161–167, http://dx.doi.org/10.1016/j.polymer.2015.08.033.
- [10] S. Wada, R. Zhang, S.R. Mannava, V.K. Vasudevan, D. Qian, Simulation-based prediction of cyclic failure in rubbery materials using nonlinear space-time finite element method coupled with continuum damage mechanics, Finite Elem. Anal. Des. 138 (2018) 21–30, http://dx.doi.org/10.1016/j.finel.2017.10.003.
- [11] C. Wu, M. Koishi, Three-dimensional meshfree-enriched finite element formulation for micromechanical hyperelastic modeling of particulate rubber composites, Internat. J. Numer. Methods Engrg. 91 (2012) 1137–1157, http://dx.doi.org/10.1002/nme.
- [12] F.W. Starr, T.B. Schrøder, S.C. Glotzer, Effects of a nanoscopic filler on the structure and dynamics of a simulated polymer melt and the relationship to ultrathin films, Phys. Rev. E 64 (2001) 5, http://dx.doi.org/10.1103/PhysRevE.64.021802.
- [13] Y. Li, M. Kröger, W.K. Liu, Nanoparticle geometrical effect on structure, dynamics and anisotropic viscosity of polyethylene nanocomposites, Macromolecules 45 (2012) 2099–2112, http://dx.doi.org/10.1021/ma202289a.
- [14] B. Arash, H.S. Park, T. Rabczuk, Mechanical properties of carbon nanotube reinforced polymer nanocomposites: A coarse-grained model, Composites B 80 (2015) 92–100, http://dx.doi.org/10.1016/j.compositesb.2015.05.038.

- [15] B. Arash, H.S. Park, T. Rabczuk, Tensile fracture behavior of short carbon nanotube reinforced polymer composites: A coarse-grained model, Compos. Struct. 134 (2015) 981–988, http://dx.doi.org/10.1016/j.compstruct.2015.09.001.
- [16] C. Shi, H. Fan, S. Li, Interphase model for effective moduli of nanoparticle-reinforced composites, J. Eng. Mech. 141 (2015) 04015052, http://dx.doi.org/10.1061/(asce)em.1943-7889.0000958.
- [17] C. Shi, Q. Tu, H. Fan, C.A.O. Rios, S. Li, Interphase models for nanoparticle-polymer composites, J. Nanomec. Micromech. 6 (2016) 04016003, http://dx.doi.org/10.1061/(asce)nm.2153-5477.0000107.
- [18] H. Jinnai, Y. Shinbori, T. Kitaoka, K. Akutagawa, N. Mashita, T. Nishi, Three-dimensional structure of a nanocomposite material consisting of two kinds of nanofillers and rubbery matrix studied by transmission electron microtomography, Macromolecules 40 (2007) 6758–6764, http://dx.doi.org/10.1021/ma071102d.
- [19] H. Jinnai, R.J. Spontak, T. Nishi, Transmission electron microtomography and polymer nanostructures, Macromolecules 43 (2010) 1675–1688, http://dx.doi.org/10.1021/ma902035p.
- [20] H. Moulinec, P. Suquet, A numerical method for computing the overall response of nonlinear composites with complex microstructure, Comput. Methods Appl. Mech. Engrg. 157 (1998) 69–94, http://dx.doi.org/10.1016/S0045-7825(97)00218-1.
- [21] B. Figliuzzi, D. Jeulin, M. Faessel, F. Willot, M. Koishi, N. Kowatari, Modelling the microstructure and the viscoelastic behaviour of carbon black filled rubber materials from 3D simulations, Tech. Mech. 32 (2016) 22–46.
- [22] V. Gallican, R. Brenner, Homogenization estimates for the effective response of fractional viscoelastic particulate composites, Contin. Mech. Thermodyn. (2018) 1–18.
- [23] Z. Liu, J.A. Moore, W.K. Liu, An extended micromechanics method for probing interphase properties in polymer nanocomposites, J. Mech. Phys. Solids 95 (2016) 663–680, http://dx.doi.org/10.1016/j.jmps.2016.05.002.
- [24] M.L. Williams, R.F. Landel, J.D. Ferry, Mechanical properties of substances of high molecular weight 19. The temperature dependence of relaxation mechanisms in Amorphous polymers and other glass-forming liquids, J. Am. Chem. Soc. 77 (1955) 3701–3707, http://dx.doi.org/10.1021/ja01619a008.
- [25] N. Kawase, M. Kato, H. Nishioka, H. Jinnai, Transmission electron microtomography without the "missing wedge" for quantitative structural analysis, Ultramicroscopy 107 (2007) 8–15.
- [26] J.C. Michel, H. Moulinec, P. Suquet, Effective properties of composite materials with periodic microstructure: A computational approach, Comput. Methods Appl. Mech. Engrg. 172 (1999) 109–143, http://dx.doi.org/10.1016/S0045-7825(98)00227-8.
- [27] M. Kabel, T. Böhlke, M. Schneider, Efficient fixed point and Newton-Krylov solvers for FFT-based homogenization of elasticity at large deformations, Comput. Mech. 54 (2014) 1497–1514, http://dx.doi.org/10.1007/s00466-014-1071-8.
- [28] H. Moulinec, P. Suquet, Comparison of FFT-based methods for computing the response of composites with highly contrasted mechanical properties, Phys. B Condens. Matter 338 (2003) 58–60, http://dx.doi.org/10.1016/S0921-4526(03)00459-9.
- [29] T.W.J. de Geus, J. Vondřejc, J. Zeman, R.H.J. Peerlings, M.G.D. Geers, Finite strain FFT-based non-linear solvers made simple, Comput. Methods Appl. Mech. Engrg. 318 (2017) 412–430, http://dx.doi.org/10.1016/j.cma.2016.12.032.
- [30] Z. Liu, M.A. Bessa, W.K. Liu, Self-consistent clustering analysis: An efficient multi-scale scheme for inelastic heterogeneous materials, Comput. Methods Appl. Mech. Engrg. 306 (2016) 319–341, http://dx.doi.org/10.1016/j.cma.2016.04.004.
- [31] Z. Liu, O.L. Kafka, C. Yu, W.K. Liu, Data-driven self-consistent clustering analysis of heterogeneous materials with crystal plasticity, in: Adv. Comput. Plast., Springer, 2018.
- [32] Z. Liu, M. Fleming, W. Kam, Microstructural material database for self-consistent clustering analysis of elastoplastic strain softening materials, Comput. Methods Appl. Mech. Engrg. 330 (2018) 547–577, http://dx.doi.org/10.1016/j.cma.2017.11.005.